

UC-NeRF: NEURAL RADIANCE FIELD FOR UNDER-CALIBRATED MULTI-VIEW CAMERAS IN AUTONOMOUS DRIVING

Kai Cheng¹, Xiaoxiao Long^{2*}, Wei Yin³, Jin Wang¹, Zhiqiang Wu², Yuexin Ma⁴,
Kaixuan Wang³, Xiaozhi Chen³, Xuejin Chen^{1†}

¹ University of Science and Technology of China

² PKU-Wuhan Institute for Artificial Intelligence

³ DJI Technology

⁴ ShanghaiTech University

ABSTRACT

Multi-camera setups find widespread use across various applications, such as autonomous driving, as they greatly expand sensing capabilities. Despite the fast development of Neural radiance field (NeRF) techniques and their wide applications in both indoor and outdoor scenes, applying NeRF to multi-camera systems remains very challenging. This is primarily due to the inherent under-calibration issues in multi-camera setup, including inconsistent imaging effects stemming from separately calibrated image signal processing units in diverse cameras, and system errors arising from mechanical vibrations during driving that affect relative camera poses. In this paper, we present UC-NeRF, a novel method tailored for novel view synthesis in under-calibrated multi-view camera systems. Firstly, we propose a layer-based color correction to rectify the color inconsistency in different image regions. Second, we propose virtual warping to generate more viewpoint-diverse but color-consistent virtual views for color correction and 3D recovery. Finally, a spatiotemporally constrained pose refinement is designed for more robust and accurate pose calibration in multi-camera systems. Our method not only achieves state-of-the-art performance of novel view synthesis in multi-camera setups, but also effectively facilitates depth estimation in large-scale outdoor scenes with the synthesized novel views. See the project page for code, data: <https://kcheng1021.github.io/ucnerf.github.io/>.

1 INTRODUCTION

Neural radiance field (NeRF) is a revolutionary approach that enables the synthesis of highly detailed and photorealistic 3D scenes from 2D images. This technology has opened up a multitude of new possibilities in autonomous driving, such as generating synthetic data from diverse viewpoints for robust training of perception models and providing effective 3D scene representations to enhance comprehensive environmental understanding (Fu et al. (2022); Zhang et al. (2023)).

Multi-camera systems (Sun et al. (2020); Caesar et al. (2020); Guizilini et al. (2020)) are commonly used for autonomous driving, while involving the strategic placement of multiple cameras to capture a holistic perspective of the surrounding environment, as shown in Fig. 1, supplying spatially consistent information to complement the temporal data for perception tasks (Mei et al. (2022); Pang et al. (2023)). Incorporating NeRF in multi-camera systems could provide a way to efficiently and economically produce extensive high-quality video data for training various models in autonomous driving systems.

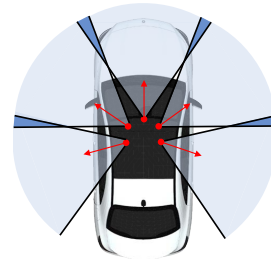


Figure 1: Illustration of a multi-camera system.

*First two authors contributed equally.

†Corresponding author (xjchen99@ustc.edu.cn).

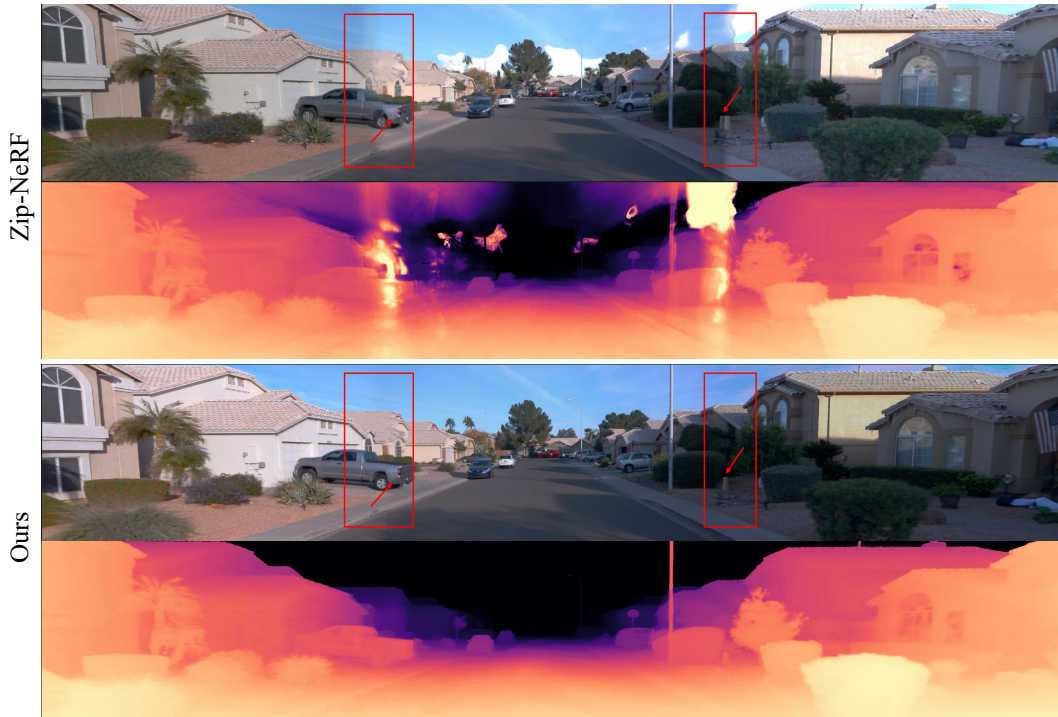


Figure 2: In under-calibrated multi-camera systems, the NeRF quality significantly degrades (the first row), along with color discrepancies (red boxes), object ghosts (red arrows), and wrong geometry (the second row). Our UC-NeRF achieves high-quality rendering and accurate geometry in the challenging cases.

However, naively combining images captured from multi-camera systems into NeRF’s training often results in a significant deterioration of rendering quality, as depicted in the first two rows of Fig. 2. The underlying cause of this degradation is the inconsistent color supervision from different views, since the multi-cameras are usually under-calibrated. This under-calibration issue manifests in two distinct ways. First, the image signal processing (ISP) units involve various techniques like white balance correction, gamma correction, etc., to convert the raw data captured by the sensors to discretized pixel colors. However, these ISP units fluctuate over time across different cameras, resulting in color disparities within the same scene region, as shown in the red box in Fig. 2. Secondly, even with delicate camera pose calibration beforehand, systematic errors during vehicle production and vibrations during driving inevitably introduce misalignment and further exacerbate color inconsistency, as indicated by the arrows in Fig. 2.

Several NeRF methods (Martin-Brualla et al. (2021); Rematas et al. (2022); Tancik et al. (2022)) attempt to alleviate the inconsistent color supervision by modeling image-dependent appearance with a global latent code for each image. However, the capacity of a global latent code to uniformly correct colors in different regions of an image is limited, especially when different regions correspond to different color transformations. Furthermore, learning one color correction for each image can lead to overfitting when the training images lack color and viewpoint diversity. This limitation is pronounced for areas observed by side-view cameras, which have fewer observations and limited overlapping with front-view areas. To correct inaccurate poses, some approaches perform joint NeRF optimization with pose refinement using photometric losses. Unfortunately, utilizing such joint optimization under a multi-camera setup, the photometric consistency across cameras can not be ensured and spatial relations among cameras are not fully utilized, making optimization more challenging and prone to local minima.

To address these challenges, we introduce UC-NeRF, a method for high-quality neural rendering with multiple under-calibrated cameras. We introduce three key innovations: 1) **Layer-based Color Correction**. To address color inconsistencies in the training images, especially for those taken by

different cameras, we design a novel layer-based color correction module. This module separately adjusts the colors of the foreground and sky regions using two learned affine transformations for each image. 2) **Virtual Warping**. We introduce a “virtual warping” strategy that generates viewpoint-diverse yet color-consistent observations for each camera at each moment. These warped images under virtual viewpoints offer stronger constraints on the latent codes for color correction, especially for multi-camera systems where the overlapping region between cameras is limited. Moreover, the virtual warping strategy naturally expands the range of the training views for NeRF, enhancing its effectiveness in learning both the scene’s appearance and geometry. 3) **Spatiotemporally Constrained Pose Refinement**. We propose a spatiotemporally constrained pose optimization strategy that explicitly models the spatial and temporal connections between cameras for pose optimization. This approach also improves the robustness against photometric differences by utilizing reprojection errors during pose optimization.

Experiments on the public datasets Waymo (Sun et al. (2020)) and NuScenes (Caesar et al. (2020)) show that our method achieves high-quality renderings with a multi-camera system and outperforms other baselines by a large margin. Moreover, we show that the obtained high-quality renderings of novel views can facilitate downstream perception tasks like depth estimation.

2 RELATED WORK

Multi-view Stereo Multi-view stereo (MVS) is a fundamental 3D vision task that aims to reconstruct a 3D model from posed images. Traditional methods (Campbell et al. (2008); Furukawa & Ponce (2009); Bleyer et al. (2011); Furukawa et al. (2015); Schönberger et al. (2016)) exploit pixel correspondences between images from hand-crafted features to infer 3D structure. Deep learning methods (Yao et al. (2018); Vakalopoulou et al. (2018); Long et al. (2020); Chen et al. (2019); Long et al. (2021); Ma et al. (2022); Feng et al. (2023)) generally build multi-view correspondences implicitly and regress the 3D scenes as depth maps or 3D volumes in an end-to-end framework. Despite the increasing capability of MVS techniques in reconstructing accurate 3D models, it is strenuous to integrate 3D models into the traditional rendering pipeline to achieve photorealistic rendering.

NeRF for Outdoor Scenes NeRF (Mildenhall et al. (2021)) is a revolutionary technology that allows for the rendering of realistic images without the prerequisite of explicitly reconstructing 3D models. It has demonstrated its effectiveness in high-quality novel view synthesis on indoor scenes and small-scale outdoor scenes. But it faces challenges when applied to unbounded outdoor scenes due to infinite depth range, complex illumination, and dynamic objects. To make NeRF more effective for infinite depth range, NeRF++ (Zhang et al. (2020)) divides the scene space into foreground and background regions with an inverted sphere parameterization. In the following works (Barron et al. (2022); Wang et al. (2023a)), more complicated non-linear scene parameterization is proposed to model the outdoor space more compactly and sample points more efficiently. Some other works (Deng et al. (2022); Xie et al. (2023); Wang et al. (2023b); Yang et al. (2023)) learn the complex geometry of outdoor scenes by introducing depth and surface normal priors. Moreover, to adapt to the view-dependent appearance due to surface reflection, camera parameters, and environment change, several works (Martin-Brualla et al. (2021); Rematas et al. (2022); Tancik et al. (2022); Turki et al. (2022); Li et al. (2023)) learn appearance-related latent codes independently to control the view-dependent effect. Besides, some works (Xie et al. (2023); Turki et al. (2023)) model dynamic objects separately based on semantic priors, using 3D detection or semantic segmentation. In comparison, we primarily address the rendering quality deterioration problem caused by under-calibration of photometry and poses in a multi-camera setup for large-scale outdoor scenes.

NeRF with Pose Refinement NeRF methods always require accurate camera poses to optimize a neural 3D scene. However, the camera poses obtained from Structure-from-Motion (SfM) usually contain subtle errors that could significantly degrade the quality of the reconstructed NeRF. NeRF-- (Wang et al. (2021)) jointly optimizes camera parameters with NeRF training via the photometric loss. However, pose optimization struggles to achieve effective updates due to the increased non-linearity of NeRF arising from position encoding. BARF (Lin et al. (2021)) eliminates this negative impact with a coarse-to-fine training strategy. SiNeRF (Xia et al. (2022)) and GARF (Shi et al. (2022)) replace the positional encoding with different activation functions to reduce non-linearity while maintaining the same rendering quality. Besides, SCNeRF (Jeong et al. (2021)) and SPARF (Truong et al. (2023)) propose different geometric losses to improve the pose accuracy further. However, directly employing these methods in multi-camera systems will lead to a bottleneck, since the

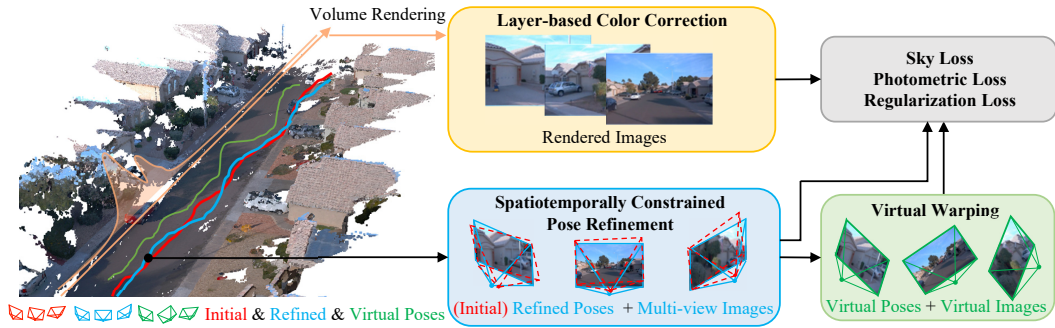


Figure 3: Overview of UC-NeRF framework. To mitigate the inconsistency of color supervision in multi-camera systems, the spatiotemporally constrained pose refinement module optimizes poses and the layer-based color correction module models the image-dependent appearance from varying cameras and timestamps. The virtual warping module generates diverse virtual views with geometric and color consistency, enriching data for color correction and 3D scene recovery.

spatial relation between cameras is not taken into consideration. MC-NeRF (Gao et al. (2023)) is a contemporaneous work on multi-camera systems, but it focuses on optimizing the intrinsics of different cameras during pose optimization while we propose the spatiotemporal constraint between different cameras to enhance pose optimization.

3 METHOD

Our UC-NeRF extends the general NeRF algorithm to the multi-camera setup in autonomous driving. We begin by reviewing the common NeRF pipeline. Then we introduce the layer-based color correction (Sec. 3.2) to reformulate the color rendering for handling the inconsistent color supervision in multi-camera systems. In Sec. 3.3, we introduce our virtual warping strategy to assist color correction by generating viewpoint-diverse but color-consistent images. Finally, the spatiotemporally constrained pose refinement is explained in Sec. 3.4.

3.1 PRELIMINARY

NeRF models a 3D scene as a continuous implicit function θ and regresses the density σ and color $\mathbf{c} \in \mathbb{R}^3$ of every individual 3D point given its 3D coordinate $\mathbf{p} \in \mathbb{R}^3$ and a unit-norm viewing direction $\mathbf{d} \in \mathbb{R}^2$. To synthesize a 2D image, NeRF employs volume rendering which samples a sequence of 3D points along a camera ray \mathbf{r} as $\mathbf{I}(\mathbf{r}) = \sum_{n=1}^N T_n \alpha_n \mathbf{c}_n$, where T_n is the accumulated transmittance of the sampled points, α_n and \mathbf{c}_n is the alpha value and the color of the sampled n -th point. Detailed definitions can be referred to NeRF (Mildenhall et al. (2021)).

To optimize NeRF, the photometric loss between the rendered color $\mathbf{I}(\mathbf{r})$ and the ground truth color $\hat{\mathbf{I}}(\mathbf{r})$ from a set of sampled rays \mathcal{R} is applied as:

$$\mathcal{L}_{\text{pho}}(\theta) = \sum_{\mathbf{r} \in \mathcal{R}} \left\| \hat{\mathbf{I}}(\mathbf{r}) - \mathbf{I}(\mathbf{r}) \right\|_2^2. \quad (1)$$

3.2 LAYER-BASED COLOR CORRECTION

In multi-camera systems, different cameras always have distinct Image Signal Processor (ISP) configurations, resulting in inconsistent imaging colors for the same 3D region. As a result, optimizing a NeRF representation using such inconsistent images always causes low-quality renderings. The work Urban-NeRF (Rematas et al. (2022)) attempts to approximate a global linear compensation transformation for each view to alleviate the discrepancies of the views from different cameras. It’s worth noticing that due to the non-linear property of the ISP process, the pixels with different intensities in a single image even have various ISP imaging effects, so it is insufficient to model these spatially varying color patterns using a single global compensation transformation. To balance

quality and efficiency, we propose to split the scene into foreground-sky layers and model the color compensation transformation for each layer separately. This is because the sky regions are always much brighter than the foreground objects, and they present distinct ISP imaging effects.

We first model the foreground and sky as two independent NeRF models θ_{fg} and θ_{sky} . The color of a rendered pixel from ray \mathbf{r} is obtained by the weighted combination of foreground color $\mathbf{I}_{fg}(\mathbf{r})$ and sky color $\mathbf{I}_{sky}(\mathbf{r})$, as illustrated in Eq. 2:

$$\mathbf{I}(\mathbf{r}) = \mathbf{I}_{fg}(\mathbf{r}) + (1 - o_{fg})\mathbf{I}_{sky}(\mathbf{r}), \quad (2)$$

where $o_{fg} = \sum_{n=1}^N T_{n,fg} \alpha_{n,fg}$ is the accumulated weight of foreground NeRF in \mathbf{r} . To encourage o_{fg} approaches 1 in the foreground area while approaches 0 in the sky area, a binary cross-entropy loss is employed as Eq. 3:

$$L_{sky}(o_{fg}, m_{sky}) = -m_{sky} \log(1 - o_{fg}) - (1 - m_{sky}) \log(o_{fg}), \quad (3)$$

where m_{sky} is the sky mask generated from pretrained segmentation model (Yin et al. (2022)).

After modeling the foreground and sky NeRF, we approximate the color correction of the foreground and the sky using separate affine transformations. Considering the color variance across both cameras and timestamps, for each training image $\mathbf{I}_{i,k}$ from camera k at timestamp i , a foreground correction code and a sky correction code are assigned to represent the image-dependent color variation (*Subscripts i, k are omitted in the following descriptions for clarity*). These correction codes are further decoded by a multi-layer perceptron (MLP) as the affine transformations $[\mathbf{A}, \mathbf{x}]$ and $[\mathbf{C}, \mathbf{y}]$, where $\mathbf{A}, \mathbf{C} \in \mathbb{R}^{3 \times 3}$, and $\mathbf{x}, \mathbf{y} \in \mathbb{R}^{3 \times 1}$. For the rendered pixel which emits \mathbf{r} in \mathbf{I} , the final pixel color in Eq. 2 can be rewritten as:

$$\mathbf{I}(\mathbf{r}) = \mathbf{A}\mathbf{I}_{fg}(\mathbf{r}) + \mathbf{x} + (1 - o_{fg})(\mathbf{C}\mathbf{I}_{sky}(\mathbf{r}) + \mathbf{y}). \quad (4)$$

To stabilize the optimization process and ensure that the adjusted color does not significantly deviate from the origin, we add a regularization term, as illustrated in Eq. 5:

$$L_{reg} = |\mathbf{A} - \mathbf{E}_3| + |\mathbf{C} - \mathbf{E}_3| + |\mathbf{x}| + |\mathbf{y}|, \quad (5)$$

where \mathbf{E}_3 refers to the identity matrix.

3.3 VIRTUAL WARPING

In multi-camera systems, images from different viewpoints often have limited overlapping areas, making it more challenging to align their colors compared to aligning frames from a single camera. To align the image colors of multiple cameras and prevent the optimized latent codes for color correction from overfitting to a specific viewpoint, we propose virtual warping, which simulates more diverse yet color-consistent images under a set of virtual viewpoints for training. Furthermore, virtual warping naturally expands the range of perspectives available to NeRF, thereby enhancing its capability to reconstruct the 3D scene. Fig. 4 shows the pipeline of our virtual warping strategy. We employ an MVS method (Ma et al. (2022)) to generate depth maps of all views. To remove outliers and retain the consistent depths across multiple views, we further leverage a geometric consistent check process (Schönberger et al. (2016)) to generate a mask \mathbf{M} that only keeps reliable depth values in each view.

With estimated depths, we generate multiple virtual poses and warp colors and color correction codes to the virtual positions. Specifically, we perturb an existing pose \mathbf{T}_o with an additional transformation $[\mathbf{R}_{o \rightarrow v}, \mathbf{t}_{o \rightarrow v}]$ as a virtual pose \mathbf{T}_v . The rotation $\mathbf{R}_{o \rightarrow v}$ is generated by randomly selecting one of the three axes with a random angle $\in [-20^\circ, 20^\circ]$. The translation $\mathbf{t}_{o \rightarrow v}$ is a 3D vector of random direction with a length $\in [0m, 1m]$. Each pixel \mathbf{p}_o in an existing image taken under camera pose \mathbf{T}_o is warped to an image point \mathbf{p}_v with the virtual pose \mathbf{T}_v as:

$$d_v \bar{\mathbf{p}}_v = \mathbf{K}(\mathbf{R}_{o \rightarrow v} \mathbf{K}^{-1} d_o \bar{\mathbf{p}}_o + \mathbf{t}_{o \rightarrow v}), \quad (6)$$

where $\bar{\mathbf{p}}_o$ and $\bar{\mathbf{p}}_v$ is the homogeneous coordinates of \mathbf{p}_o and \mathbf{p}_v , \mathbf{K} is the camera intrinsic matrix, d_v and d_o are the pixel depth in the virtual view and the corresponding pixel depth in the original real view. Considering object occlusions, there could be multiple pixels in the original views mapped to the same position in the virtual view, so we keep the warped pixel with the minimum depth.

After warping, the geometric consistency mask \mathbf{M} is applied to the warped pixels to filter pixels with noisy depth. Then the color and the color correction code of the pixel in the original view are assigned to the corresponding warped pixels in the virtual view. This provides more clues to recover the consistent appearance and geometry of the scene.

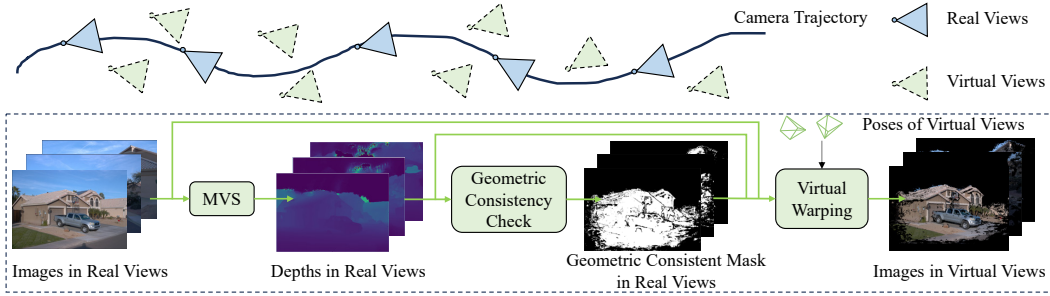


Figure 4: The generation of virtual warped images. For each known viewpoint, we generate its depth map using MVS and filter out inaccurate depths through a geometric consistency check. Each virtual view is obtained by warping the image from a known viewpoint to the virtual viewpoint.

3.4 SPATIOTEMPORALLY CONSTRAINED POSE REFINEMENT

The rendering quality of NeRF heavily relies on the accuracy of camera poses. Previous approaches (Tancik et al. (2022); Xie et al. (2023)) model the camera poses independently and jointly optimize them within the NeRF framework. They do not fully exploit the spatial correlations between cameras in multi-camera systems, leading to under-constrained pose optimization. Additionally, the camera pose optimization depends on the photometric consistency assumption, which is usually violated in long-time videos captured in multi-camera systems. Given the condition that the cameras have a fixed spatial relationship with the main capturing device (i.e. the driving car) during the whole process, we explicitly establish the temporally fixed geometric transformation between cameras.

While capturing multi-view images with K cameras, the pose \mathbf{T}_k^i of the k th camera at time i is denoted as the combination of the car’s ego pose \mathbf{T}^i and the relative transformation $\Delta\mathbf{T}_k$, which is temporally consistent and optimizable, as Fig. 5 shows. Explicitly modeling the spatial relationship between cameras provides more restrictions for pose refinement, thus effectively enhancing robustness against incorrect point matches across all frames.

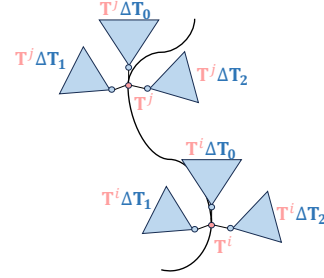


Figure 5: Pose modeling.

After building the spatio-temporal constraint between camera poses, point correspondences between images captured by different cameras at different times are established as correlation graph \mathcal{E} . Then we employ bundle adjustment to minimize the reprojection error defined as:

$$L_{rpj} = \sum_{((i,k),(j,l)) \in \mathcal{E}} \left\| \mathbf{p}_l^j - \Pi_l \left((\mathbf{T}^j \Delta\mathbf{T}_l)^{-1} \mathbf{T}^i \Delta\mathbf{T}_k \Pi_k^{-1} (\mathbf{q}_k^i) \right) \right\|^2, \quad (7)$$

where \mathbf{p}_l^j and \mathbf{q}_k^i are pixels in the images captured by camera l at time j and camera k at time i , Π_l and Π_k^{-1} are projection function of camera l and unprojection function of camera k .

3.5 TRAINING STRATEGY

Our training strategy mainly includes two parts: 1) Pose refinement and depth estimation. We initialize the poses from sensor-fusion SLAM and further optimize them using our proposed spatiotemporally constrained pose refinement module, as described in Eq. 7. With these refined poses, we generate a depth map and geometric consistency mask for each image, following the procedure outlined in Sec. 3.3. 2) End-to-end NeRF optimization. Specifically, the proposed layer-based color correction and virtual warping are used in the optimization of NeRF to achieve high-quality renderings. In each training batch, we randomly sample B real images and employ our virtual warping module to create V virtual views for each real image. The pixels are randomly sampled from these real and virtual views as the ground truth for NeRF training. Our UCNeRF renders these pixels based on Eq. 4 and is supervised by the loss function in Eq. 8:

Table 1: Comparison on Waymo and NuScenes. Our method significantly outperforms state-of-the-art methods in both datasets and all the evaluation metrics.

Method	Waymo			NuScenes		
	PSNR \uparrow	SSIM \uparrow	LPIPS \downarrow	PSNR \uparrow	SSIM \uparrow	LPIPS \downarrow
Mip-NeRF (Barron et al. (2021))	22.42	0.698	0.471	23.31	0.758	0.489
Mip-NeRF 360 (Barron et al. (2022))	24.46	0.769	0.406	25.15	0.809	0.436
Instant-NGP (Müller et al. (2022))	23.84	0.702	0.494	23.81	0.777	0.476
S-NeRF (Xie et al. (2023))	24.89	0.772	0.401	26.02	0.824	0.415
Zip-NeRF (Barron et al. (2023))	26.21	0.815	0.389	27.06	0.831	0.435
UC-NeRF (Ours)	28.13	0.842	0.356	30.20	0.876	0.374

$$L = L_{pho} + \lambda L_{sky} + \gamma L_{reg}, \quad (8)$$

where λ and γ are the weights of L_{sky} and L_{reg} .

4 EXPERIMENTS

4.1 DATASETS AND IMPLEMENTATION DETAILS

Datasets. We conduct our experiments in two urban datasets which contain images captured from multi-cameras, *i.e.*, Waymo (Sun et al. (2020)) and NuScenes (Caesar et al. (2020)). We select ten static scenes in Waymo and five static scenes in NuScenes for evaluation. To evaluate the performance of novel view synthesis, following common settings, we select one of every eight images of each camera as testing images and the remaining ones as training data. We apply the three widely-used metrics for evaluation, *i.e.*, peak signal-to-noise ratio (PSNR), structural similarity index measure (SSIM), and the learned perceptual image patch similarity (LPIPS) (Zhang et al. (2018)).

Baselines. We choose Zip-NeRF (Barron et al. (2023)) as our baseline. Since there is no official code for Zip-NeRF, we use the reimplementation of Zip-NeRF in Gu (2023). We compare our method with the baseline and other state-of-the-art NeRF methods, including Mip-NeRF (Barron et al. (2021)), Mip-NeRF 360 (Barron et al. (2022)), Instant-NGP (Müller et al. (2022)), and S-NeRF (Xie et al. (2023)). We provide implementation details in the appendix.

4.2 RESULTS ON NOVEL VIEW SYNTHESIS

The comparison result of neural rendering in urban scenes with a multi-camera setting is shown in Tab. 1. With the proposed layer-based color correction, virtual warping, and spatio-temporally constrained pose refinement, our UC-NeRF outperforms the other methods in both datasets. We also show the panoramic rendering results in Fig. 6. Without any anti-aliasing design in the rendering process, images generated by Instant-NGP and S-NeRF exhibit notable blurriness. Although Zip-NeRF features an anti-aliasing mechanism, it also amplifies the artifacts caused by inconsistent color supervision across different views. Our approach excels at rendering consistent colors and sharp details, as highlighted in the regions of texts, cars, and buildings. Additionally, our method provides more accurate 3D reconstruction, as demonstrated by the depth maps. We show more results on Waymo and NuScenes in the appendix.

4.3 ABLATION STUDY

We conduct extensive ablation studies on ten scenes from the Waymo dataset to explore the effect of each proposed module in our UC-NeRF. We investigate the effect of each module, *i.e.*, layer-based color correction (LCC), spatiotemporally constrained pose refinement (STPR), and virtual warping (VW). As shown

Table 2: Ablation study.

	LCC	STPR	VW	PSNR \uparrow	SSIM \uparrow	LPIPS \downarrow
	\times	\times	\times	26.21	0.815	0.389
	\times	\checkmark	\times	26.95	0.839	0.360
	\checkmark	\times	\times	27.18	0.820	0.375
	\checkmark	\times	\checkmark	27.26	0.825	0.372
	\checkmark	\checkmark	\times	27.82	0.838	0.371
	\checkmark	\checkmark	\checkmark	28.13	0.842	0.356

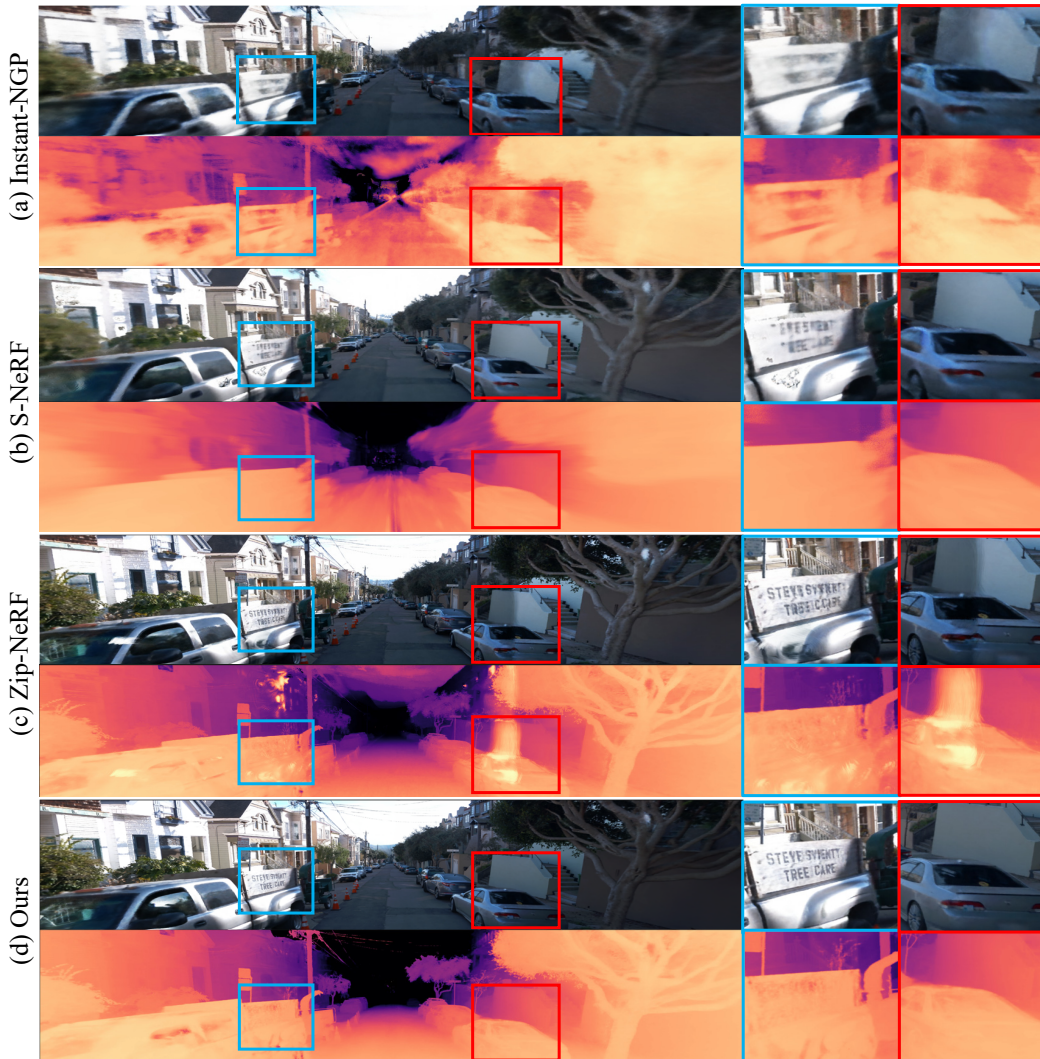


Figure 6: We render the panoramas at a resolution of 5760×1280 for comparison. Notable enhancements are indicated in blue and red boxes, and cropped patches are displayed to emphasize specific details. Compared to other methods, our results present consistent color and sharp details, even faithfully recovering the slogans. For additional results, please refer to the appendix.

in Tab. 2, the layer-based color correction module brings significant improvement (the third row) compared with the baseline model, since it solves the problem of inconsistent color supervision between views in training. Fig. 7 (b) also illustrates that the LCC module reduces hazy artifacts and presents sharper renderings. By incorporating the spatiotemporally constrained pose refinement (STPR) module, the quality of rendering is further improved. Moreover, our virtual warping (VW) strategy can enrich the diversity of training views for learning color correction, appearance, and geometry. Even the object details, e.g. the car lights and the car emblem, become more discernible in Fig. 7 (d). One notable thing is that the accuracy of the virtual views provided by virtual warping is closely related to the accuracy of the poses. Thus, virtual warping provides a more noticeable boost when the pose refinement module is added (the fourth and sixth row in Tab. 2). More detailed discussions can be referred to in the appendix.

Benefits of Virtual Warping Virtual warping enriches NeRF’s training perspectives of each camera by generating images with consistent geometry and photometry. In addition to the overall improvement in rendering quality shown in Tab. 2, we present more cases demonstrating a significant

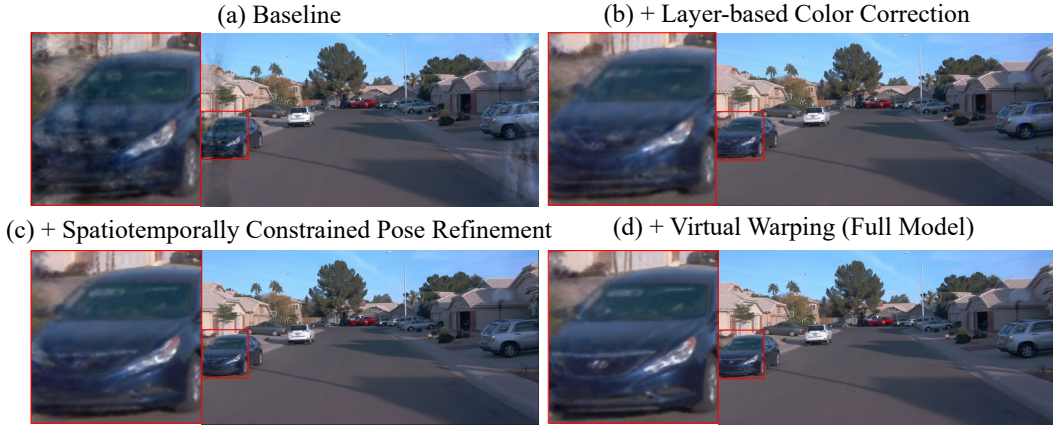


Figure 7: Each proposed module progressively enhances the rendering quality of novel views.



Figure 8: Virtual warping benefits color correction (top) and edge sharpness (bottom).

enhancement in rendering quality after incorporating virtual warping in Fig. 8. This includes better color correction (the first row) and enhanced image details (the second row).

Efficiency Analysis We compare the efficiency of different methods in Tab. 3. All methods are tested on one NVIDIA Tesla V100 GPU with an image resolution of 1920×1280 . Note that our training time includes both steps (pose refinement and NeRF training) described in Sec. 3.5. Zip-NeRF is more efficient than other methods except Instant-NGP, which is specifically designed for NeRF acceleration. Since our method is built upon Zip-NeRF, our method consumes a bit more time than Zip-NeRF but achieves a significant improvement in rendering quality.

Table 3: Efficiency Analysis. Tested on one NVIDIA Tesla V100 GPU with image resolution 1920×1280 .

Method	Training	Inference	PSNR
Mip-NeRF (Barron et al. (2021))	20h	70s	22.42
Mip-NeRF-360 (Barron et al. (2022))	14h	42s	24.46
Instant-NGP (Müller et al. (2022))	30min	0.35s	23.84
S-NeRF (Xie et al. (2023))	15h	80s	24.89
Zip-NeRF (Barron et al. (2023))	2h	2s	26.21
UC-NeRF (Ours)	3h	3.2s	28.13

5 CONCLUSION AND FUTURE WORK

In conclusion, we propose UC-NeRF that effectively addresses the challenges of integrating multi-camera systems into the NeRF paradigm. Experiments on Waymo and NuScenes demonstrate a significant improvement in rendering quality, setting a new benchmark for neural rendering within multi-camera setups. Furthermore, the application of our trained NeRF for improving depth estimation has shown promising results, underscoring the high rendering quality of novel views and the potential of NeRF for downstream perception tasks. Looking forward, there are several promising avenues for future exploration. One key objective is to adapt our method to a real-time rendering

framework. This advancement would be of great value in autonomous driving, where real-time simulation and interaction are critical. Besides, the promising results obtained from depth estimation invite further exploration into the versatility of our NeRF model. It would be worthwhile to investigate if the high-quality rendering can be utilized to enrich other perception tasks, e.g. semantic segmentation and object detection, thereby broadening the scope of our model’s applications.

REFERENCES

- Jonathan T Barron, Ben Mildenhall, Matthew Tancik, Peter Hedman, Ricardo Martin-Brualla, and Pratul P Srinivasan. Mip-nerf: A multiscale representation for anti-aliasing neural radiance fields. In *Proceedings of the IEEE/CVF International Conference on Computer Vision*, pp. 5855–5864, 2021.
- Jonathan T Barron, Ben Mildenhall, Dor Verbin, Pratul P Srinivasan, and Peter Hedman. Mip-nerf 360: Unbounded anti-aliased neural radiance fields. In *Proceedings of the IEEE/CVF Conference on Computer Vision and Pattern Recognition*, pp. 5470–5479, 2022.
- Jonathan T Barron, Ben Mildenhall, Dor Verbin, Pratul P Srinivasan, and Peter Hedman. Zip-nerf: Anti-aliased grid-based neural radiance fields. *Proceedings of the IEEE/CVF International Conference on Computer Vision*, 2023.
- Michael Bleyer, Christoph Rhemann, and Carsten Rother. Patchmatch stereo-stereo matching with slanted support windows. In *Bmvc*, volume 11, pp. 1–11, 2011.
- Holger Caesar, Varun Bankiti, Alex H Lang, Sourabh Vora, Venice Erin Liong, Qiang Xu, Anush Krishnan, Yu Pan, Giancarlo Baldan, and Oscar Beijbom. nuscenes: A multimodal dataset for autonomous driving. In *Proceedings of the IEEE/CVF conference on computer vision and pattern recognition*, pp. 11621–11631, 2020.
- Neill DF Campbell, George Vogiatzis, Carlos Hernández, and Roberto Cipolla. Using multiple hypotheses to improve depth-maps for multi-view stereo. In *Computer Vision–ECCV 2008: 10th European Conference on Computer Vision, Marseille, France, October 12–18, 2008, Proceedings, Part I 10*, pp. 766–779. Springer, 2008.
- Rui Chen, Songfang Han, Jing Xu, and Hao Su. Point-based multi-view stereo network. In *Proceedings of the IEEE/CVF international conference on computer vision*, pp. 1538–1547, 2019.
- Kangle Deng, Andrew Liu, Jun-Yan Zhu, and Deva Ramanan. Depth-supervised nerf: Fewer views and faster training for free. In *Proceedings of the IEEE/CVF Conference on Computer Vision and Pattern Recognition*, pp. 12882–12891, 2022.
- Daniel DeTone, Tomasz Malisiewicz, and Andrew Rabinovich. Superpoint: Self-supervised interest point detection and description. In *Proceedings of the IEEE conference on computer vision and pattern recognition workshops*, pp. 224–236, 2018.
- Ziyue Feng, Leon Yang, Pengsheng Guo, and Bing Li. Cvrecon: Rethinking 3d geometric feature learning for neural reconstruction. *arXiv preprint arXiv:2304.14633*, 2023.
- Xiao Fu, Shangzhan Zhang, Tianrun Chen, Yichong Lu, Lanyun Zhu, Xiaowei Zhou, Andreas Geiger, and Yiyi Liao. Panoptic nerf: 3d-to-2d label transfer for panoptic urban scene segmentation. In *2022 International Conference on 3D Vision (3DV)*, pp. 1–11. IEEE, 2022.
- Yasutaka Furukawa and Jean Ponce. Accurate, dense, and robust multiview stereopsis. *IEEE transactions on pattern analysis and machine intelligence*, 32(8):1362–1376, 2009.
- Yasutaka Furukawa, Carlos Hernández, et al. Multi-view stereo: A tutorial. *Foundations and Trends® in Computer Graphics and Vision*, 9(1-2):1–148, 2015.
- Yu Gao, Lutong Su, Hao Liang, Yufeng Yue, Yi Yang, and Mengyin Fu. Mc-nerf: Muti-camera neural radiance fields for muti-camera image acquisition systems. *arXiv preprint arXiv:2309.07846*, 2023.

-
- Chun Gu. Zipnerf-pytorch, 2023. URL <https://github.com/SuLvXiangXin/zipnerf-pytorch>. Accessed: 2023-04-23.
- Vitor Guizilini, Rares Ambrus, Sudeep Pillai, Allan Raventos, and Adrien Gaidon. 3d packing for self-supervised monocular depth estimation. In *Proceedings of the IEEE/CVF conference on computer vision and pattern recognition*, pp. 2485–2494, 2020.
- Yoonwoo Jeong, Seokjun Ahn, Christopher Choy, Anima Anandkumar, Minsu Cho, and Jaesik Park. Self-calibrating neural radiance fields. In *Proceedings of the IEEE/CVF International Conference on Computer Vision*, pp. 5846–5854, 2021.
- Peihao Li, Shaohui Wang, Chen Yang, Bingbing Liu, Weichao Qiu, and Haoqian Wang. Nerfms: Neural radiance fields with multi-sequence. In *Proceedings of the IEEE/CVF International Conference on Computer Vision*, pp. 18591–18600, 2023.
- Chen-Hsuan Lin, Wei-Chiu Ma, Antonio Torralba, and Simon Lucey. Barf: Bundle-adjusting neural radiance fields. In *Proceedings of the IEEE/CVF International Conference on Computer Vision*, pp. 5741–5751, 2021.
- Ce Liu, Suryansh Kumar, Shuhang Gu, Radu Timofte, and Luc Van Gool. Va-depthnet: A variational approach to single image depth prediction. In *The Eleventh International Conference on Learning Representations*, 2023.
- Xiaoxiao Long, Lingjie Liu, Christian Theobalt, and Wenping Wang. Occlusion-aware depth estimation with adaptive normal constraints. In *Computer Vision—ECCV 2020: 16th European Conference, Glasgow, UK, August 23–28, 2020, Proceedings, Part IX 16*, pp. 640–657. Springer, 2020.
- Xiaoxiao Long, Lingjie Liu, Wei Li, Christian Theobalt, and Wenping Wang. Multi-view depth estimation using epipolar spatio-temporal networks. In *Proceedings of the IEEE/CVF Conference on Computer Vision and Pattern Recognition*, pp. 8258–8267, 2021.
- Zeyu Ma, Zachary Teed, and Jia Deng. Multiview stereo with cascaded epipolar raft. In *European Conference on Computer Vision*, pp. 734–750. Springer, 2022.
- Ricardo Martin-Brualla, Noha Radwan, Mehdi SM Sajjadi, Jonathan T Barron, Alexey Dosovitskiy, and Daniel Duckworth. Nerf in the wild: Neural radiance fields for unconstrained photo collections. In *Proceedings of the IEEE/CVF Conference on Computer Vision and Pattern Recognition*, pp. 7210–7219, 2021.
- Jieru Mei, Alex Zihao Zhu, Xinchun Yan, Hang Yan, Siyuan Qiao, Liang-Chieh Chen, and Henrik Kretschmar. Waymo open dataset: Panoramic video panoptic segmentation. In *European Conference on Computer Vision*, pp. 53–72. Springer, 2022.
- Ben Mildenhall, Pratul P Srinivasan, Matthew Tancik, Jonathan T Barron, Ravi Ramamoorthi, and Ren Ng. Nerf: Representing scenes as neural radiance fields for view synthesis. *Communications of the ACM*, 65(1):99–106, 2021.
- Thomas Müller, Alex Evans, Christoph Schied, and Alexander Keller. Instant neural graphics primitives with a multiresolution hash encoding. *ACM Transactions on Graphics (ToG)*, 41(4):1–15, 2022.
- Ziqi Pang, Jie Li, Pavel Tokmakov, Dian Chen, Sergey Zagoruyko, and Yu-Xiong Wang. Standing between past and future: Spatio-temporal modeling for multi-camera 3d multi-object tracking. In *Proceedings of the IEEE/CVF Conference on Computer Vision and Pattern Recognition*, pp. 17928–17938, 2023.
- Konstantinos Rematas, Andrew Liu, Pratul P Srinivasan, Jonathan T Barron, Andrea Tagliasacchi, Thomas Funkhouser, and Vittorio Ferrari. Urban radiance fields. In *Proceedings of the IEEE/CVF Conference on Computer Vision and Pattern Recognition*, pp. 12932–12942, 2022.

-
- Johannes L Schönberger, Enliang Zheng, Jan-Michael Frahm, and Marc Pollefeys. Pixelwise view selection for unstructured multi-view stereo. In *Computer Vision–ECCV 2016: 14th European Conference, Amsterdam, The Netherlands, October 11–14, 2016, Proceedings, Part III 14*, pp. 501–518. Springer, 2016.
- Yue Shi, Dingyi Rong, Bingbing Ni, Chang Chen, and Wenjun Zhang. Garf: Geometry-aware generalized neural radiance field. *arXiv preprint arXiv:2212.02280*, 2022.
- Pei Sun, Henrik Kretschmar, Xerxes Dotiwalla, Aurelien Chouard, Vijaysai Patnaik, Paul Tsui, James Guo, Yin Zhou, Yuning Chai, Benjamin Caine, et al. Scalability in perception for autonomous driving: Waymo open dataset. In *Proceedings of the IEEE/CVF conference on computer vision and pattern recognition*, pp. 2446–2454, 2020.
- Matthew Tancik, Vincent Casser, Xinchun Yan, Sabeek Pradhan, Ben Mildenhall, Pratul P Srinivasan, Jonathan T Barron, and Henrik Kretschmar. Block-nerf: Scalable large scene neural view synthesis. In *Proceedings of the IEEE/CVF Conference on Computer Vision and Pattern Recognition*, pp. 8248–8258, 2022.
- Fabio Tosi, Alessio Tonioni, Daniele De Gregorio, and Matteo Poggi. Nerf-supervised deep stereo. In *Proceedings of the IEEE/CVF Conference on Computer Vision and Pattern Recognition*, pp. 855–866, 2023.
- Prune Truong, Marie-Julie Rakotosaona, Fabian Manhardt, and Federico Tombari. Sparf: Neural radiance fields from sparse and noisy poses. In *Proceedings of the IEEE/CVF Conference on Computer Vision and Pattern Recognition*, pp. 4190–4200, 2023.
- Haithem Turki, Deva Ramanan, and Mahadev Satyanarayanan. Mega-nerf: Scalable construction of large-scale nerfs for virtual fly-throughs. In *Proceedings of the IEEE/CVF Conference on Computer Vision and Pattern Recognition*, pp. 12922–12931, 2022.
- Haithem Turki, Jason Y Zhang, Francesco Ferroni, and Deva Ramanan. Suds: Scalable urban dynamic scenes. In *Proceedings of the IEEE/CVF Conference on Computer Vision and Pattern Recognition*, pp. 12375–12385, 2023.
- Maria Vakalopoulou, Guillaume Chassagnon, Norbert Bus, Rafael Marini, Evangelia I Zacharaki, M-P Revel, and Nikos Paragios. Atlasnet: Multi-atlas non-linear deep networks for medical image segmentation. In *Medical Image Computing and Computer Assisted Intervention–MICCAI 2018: 21st International Conference, Granada, Spain, September 16–20, 2018, Proceedings, Part IV 11*, pp. 658–666. Springer, 2018.
- Peng Wang, Yuan Liu, Zhaoxi Chen, Lingjie Liu, Ziwei Liu, Taku Komura, Christian Theobalt, and Wenping Wang. F2-nerf: Fast neural radiance field training with free camera trajectories. In *Proceedings of the IEEE/CVF Conference on Computer Vision and Pattern Recognition*, pp. 4150–4159, 2023a.
- Zian Wang, Tianchang Shen, Jun Gao, Shengyu Huang, Jacob Munkberg, Jon Hasselgren, Zan Gojcic, Wenzheng Chen, and Sanja Fidler. Neural fields meet explicit geometric representations for inverse rendering of urban scenes. In *Proceedings of the IEEE/CVF Conference on Computer Vision and Pattern Recognition*, pp. 8370–8380, 2023b.
- Zirui Wang, Shangzhe Wu, Weidi Xie, Min Chen, and Victor Adrian Prisacariu. Nerf-: Neural radiance fields without known camera parameters. *arXiv preprint arXiv:2102.07064*, 2021.
- Yitong Xia, Hao Tang, Radu Timofte, and Luc Van Gool. Sinerf: Sinusoidal neural radiance fields for joint pose estimation and scene reconstruction. *arXiv preprint arXiv:2210.04553*, 2022.
- Ziyang Xie, Junge Zhang, Wenye Li, Feihu Zhang, and Li Zhang. S-nerf: Neural radiance fields for street views. In *The Eleventh International Conference on Learning Representations*, 2023.
- Ze Yang, Yun Chen, Jingkan Wang, Sivabalan Manivasagam, Wei-Chiu Ma, Anqi Joyce Yang, and Raquel Urtasun. Unisim: A neural closed-loop sensor simulator. In *Proceedings of the IEEE/CVF Conference on Computer Vision and Pattern Recognition*, pp. 1389–1399, 2023.

Yao Yao, Zixin Luo, Shiwei Li, Tian Fang, and Long Quan. Mvsnet: Depth inference for unstructured multi-view stereo. In *Proceedings of the European conference on computer vision (ECCV)*, pp. 767–783, 2018.

Wei Yin, Yifan Liu, Chunhua Shen, Anton van den Hengel, and Baichuan Sun. The devil is in the labels: Semantic segmentation from sentences. *arXiv preprint arXiv:2202.02002*, 2022.

Kai Zhang, Gernot Riegler, Noah Snavely, and Vladlen Koltun. Nerf++: Analyzing and improving neural radiance fields. *arXiv preprint arXiv:2010.07492*, 2020.

Richard Zhang, Phillip Isola, Alexei A Efros, Eli Shechtman, and Oliver Wang. The unreasonable effectiveness of deep features as a perceptual metric. In *Proceedings of the IEEE conference on computer vision and pattern recognition*, pp. 586–595, 2018.

Xiaoshuai Zhang, Abhijit Kundu, Thomas Funkhouser, Leonidas Guibas, Hao Su, and Kyle Genova. Nerflets: Local radiance fields for efficient structure-aware 3d scene representation from 2d supervision. In *Proceedings of the IEEE/CVF Conference on Computer Vision and Pattern Recognition*, pp. 8274–8284, 2023.

A APPENDIX

A.1 IMPLEMENTATION DETAILS

We train our UC-NeRF for 40k iterations using Adam optimizer with a batch size of 32384. The learning rate is logarithmically reduced from 0.008 to 0.001, with a warm-up phase consisting of 5000 iterations. The training takes about 3 hours for a scene with about 300 images on two V100 GPUs.

Layer-based Color Correction In UC-NeRF, we model a scene as the foreground and sky. The foreground is represented by Zip-NeRF while the sky is modeled by the vanilla NeRF (Mildenhall et al. (2021)). The weight of sky loss is set to 2×10^{-3} . The dimension of sky latent code and foreground latent code is set to 4. For the MLP that decodes the latent code, we use three layers with 256 hidden units. The weight of transformation regularization is set to 2×10^{-3} .

Virtual Warping For virtual warping, we randomly sample 9 virtual poses for each existing pose. The occlusion needs to be considered in the case of multiple pixels of the known view warping to the same pixel in the virtual view, which is shown in the red boxes of Fig. 9. We resolve this conflict by taking the warped pixel with the smallest depth value. For generating the geometric consistency mask, we set 6 target views to check the depth consistency. Only pixels with depth absolute relative error within the range of 0.01 for at least 4 neighboring views are retained. For each training batch, we sample the rays from the real and virtual images at a ratio of 4 : 1 respectively.

Spatiotemporally Constrained Pose Refinement We use the reprojection error to optimize the camera poses. To calculate the reprojection error, the feature points need to be extracted from images. We use Superpoint (DeTone et al. (2018)) to detect and describe the keypoints. The keypoints are matched by mutual nearest neighbors and the confidence higher than 0.95 is preserved. For each view, we match it with the subsequent ten frames captured by the same camera and the subsequent twenty frames from different cameras. Image pairs with more than 30 matching points are retained.

A.2 SPECIAL CASE FOR SPATIOTEMPORAL CONSTRAINT

In Sec. 3.4, we model the pose of k th camera at timestamp i as $\mathbf{T}_k^i = \mathbf{T}^i \Delta \mathbf{T}_k$. Here pose refers to the transformation from the camera coordinate to the world coordinate. \mathbf{T}^i refers to the car’s ego pose at time i . $\Delta \mathbf{T}_k$ refers to the transformation from the k th camera’s coordinate to the ego coordinate, which is temporally consistent. During bundle adjustment, \mathbf{T}_k^i , and \mathbf{T}_l^j are optimized as Eq. 7 in Sec. 3.4, where $(\mathbf{T}_l^j)^{-1} \mathbf{T}_k^i$ are expressed as:

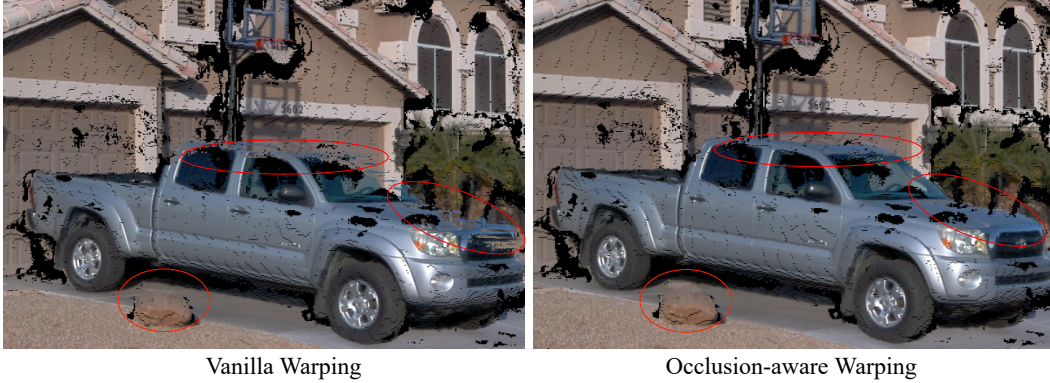


Figure 9: Occlusion problem in warping.

$$\begin{aligned}
 (\mathbf{T}_l^j)^{-1}\mathbf{T}_k^i &= (\mathbf{T}^j \Delta\mathbf{T}_l)^{-1} \mathbf{T}^i \Delta\mathbf{T}_k \\
 &= \Delta\mathbf{T}_l^{-1} (\mathbf{T}^j)^{-1} \mathbf{T}^i \Delta\mathbf{T}_k.
 \end{aligned} \tag{9}$$

Expressing $(\mathbf{T}^j)^{-1}\mathbf{T}^i = \begin{bmatrix} \mathbf{R}^{i,j} & \mathbf{t}^{i,j} \\ \mathbf{0} & \mathbf{1} \end{bmatrix}$, $\Delta\mathbf{T}_l = \begin{bmatrix} \Delta\mathbf{R}_l & \Delta\mathbf{t}_l \\ \mathbf{0} & \mathbf{1} \end{bmatrix}$, and $\Delta\mathbf{T}_k = \begin{bmatrix} \Delta\mathbf{R}_k & \Delta\mathbf{t}_k \\ \mathbf{0} & \mathbf{1} \end{bmatrix}$, then

$$\begin{aligned}
 (\mathbf{T}_l^j)^{-1}\mathbf{T}_k^i &= \begin{bmatrix} \Delta\mathbf{R}_l^\top & -\Delta\mathbf{R}_l^\top \Delta\mathbf{t}_l \\ \mathbf{0} & \mathbf{1} \end{bmatrix} \begin{bmatrix} \mathbf{R}^{i,j} & \mathbf{t}^{i,j} \\ \mathbf{0} & \mathbf{1} \end{bmatrix} \begin{bmatrix} \Delta\mathbf{R}_k & \Delta\mathbf{t}_k \\ \mathbf{0} & \mathbf{1} \end{bmatrix} \\
 &= \begin{bmatrix} \Delta\mathbf{R}_l^\top \mathbf{R}^{i,j} \Delta\mathbf{R}_k & \Delta\mathbf{R}_l^\top \mathbf{R}^{i,j} \Delta\mathbf{t}_k + \Delta\mathbf{R}_l^\top \mathbf{t}^{i,j} - \Delta\mathbf{R}_l^\top \Delta\mathbf{t}_l \\ \mathbf{0} & \mathbf{1} \end{bmatrix}.
 \end{aligned} \tag{10}$$

When the vehicle is moving straight without any rotation, $\mathbf{R}^{i,j}$ equals to the identity matrix. Thus, the Eq. 10 is simplified as:

$$(\mathbf{T}_l^j)^{-1}\mathbf{T}_k^i = \begin{bmatrix} \Delta\mathbf{R}_l^\top \Delta\mathbf{R}_k & \Delta\mathbf{R}_l^\top \Delta\mathbf{t}_k + \Delta\mathbf{R}_l^\top \mathbf{t}^{i,j} - \Delta\mathbf{R}_l^\top \Delta\mathbf{t}_l \\ \mathbf{0} & \mathbf{1} \end{bmatrix}. \tag{11}$$

If the image correspondences are not established across cameras, *i.e.*, $l = k$, then Eq. 11 can further simplified as:

$$(\mathbf{T}_l^j)^{-1}\mathbf{T}_k^i = \begin{bmatrix} \mathbf{I} & \Delta\mathbf{R}_k^\top \mathbf{t}^{i,j} \\ \mathbf{0} & \mathbf{1} \end{bmatrix}, \tag{12}$$

which suggests that the relative transformation between any two neighboring poses of the same camera k remains unaffected by $\Delta\mathbf{t}_k$, thus resulting in a lack of constraint on the camera's translation $\Delta\mathbf{t}_k$ during the optimization process. This implies that the image correspondences across both cameras and timestamps ensure a robust constraint on inter-camera transformation.

A.3 EXPERIMENTS

A.3.1 APPLICATION: SYNTHESIZED VIEWS FOR MONOCULAR DEPTH ESTIMATION

With the obtained 3D NeRF, we can generate additional photo-realistic images from novel view-points. The synthesized images can facilitate downstream perception tasks like monocular depth estimation. We first train VA-DepthNet, a state-of-the-art monocular depth estimation model (Liu et al. (2023)), on the original real images. We then train the model by combining the original real images and the new synthesized images (VA-DepthNet*). As Tab. 4 illustrates, the accuracy of the estimated depth is improved with such a data augmentation. Fig. 10 also shows such an operation leads to sharper edges and more accurate predictions.

Table 4: The accuracy of depth estimation using VA-DepthNet before and after adding our rendered novel views (VA-DepthNet*) for training.

Method	Abs Rel ↓	RMSE ↓	$\delta 1 \uparrow$
VA-DepthNet	0.078	2.82	93.7
VA-DepthNet*	0.076	2.64	94.2

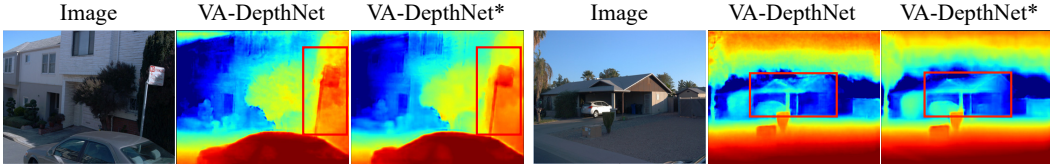


Figure 10: Compared to training VA-DepthNet (Liu et al. (2023)) on the original data, augmenting it with our rendered novel views (VA-DepthNet*) leads to improved depth estimation. Depth of VA-DepthNet* in the red boxes exhibits sharper edges and smoother surfaces.

A.3.2 MORE ABLATION STUDY RESULTS

Color Correction Strategies. We compare our color correction with other strategies that also model the image-dependent appearance with latent codes, as done in NeRF in the wild (Martin-Brualla et al. (2021)) and Urban-NeRF (Rematas et al. (2022)). As shown in Fig. 11, the baseline (a) exhibits noticeable color discontinuities in regions where camera views overlap (indicated by red arrows). Although NeRF in the wild (b) models image-dependent appearance through latent codes, the absence of constraints on latent codes results in the disentanglement of attributes not related to the cause of color inconsistency. As a result, the panoramic rendering produced by it exhibits significant blurriness on both sides (emphasized by red boxes), along with additional texture artifacts in the sky (the red arrows). Urban-NeRF (c) also decodes the latent code into affine transformations to model image-dependent appearance. However, due to the absence of separate modeling for color transformations across different image regions, color discontinuities, as indicated by the red arrows, persist in the overlapping regions of the cameras. Additionally, the lack of constraints for inter-camera color correction results in misalignment within the same color space across different regions. When employing a single latent code for rendering the panorama image, the color within the central region adheres closely to reality. However, severe color deviations occur in the peripheral area, such as the grass in the red box, which appears black instead of its natural color. In contrast, our method addresses the color inconsistencies and ensures clear details with consistent colors. Tab. 5 also demonstrates that our approach achieves the best rendering results.



Figure 11: Comparison of color correction strategies for rendering images with large field of view.

Table 5: Comparison of different strategies for color correction.

Method	PSNR \uparrow	SSIM \uparrow	LPIPS \downarrow
NeRF in the wild (Martin-Brualla et al. (2021))	25.59	0.839	0.389
Urban-NeRF (Rematas et al. (2022))	27.89	0.849	0.378
Ours	28.15	0.851	0.374

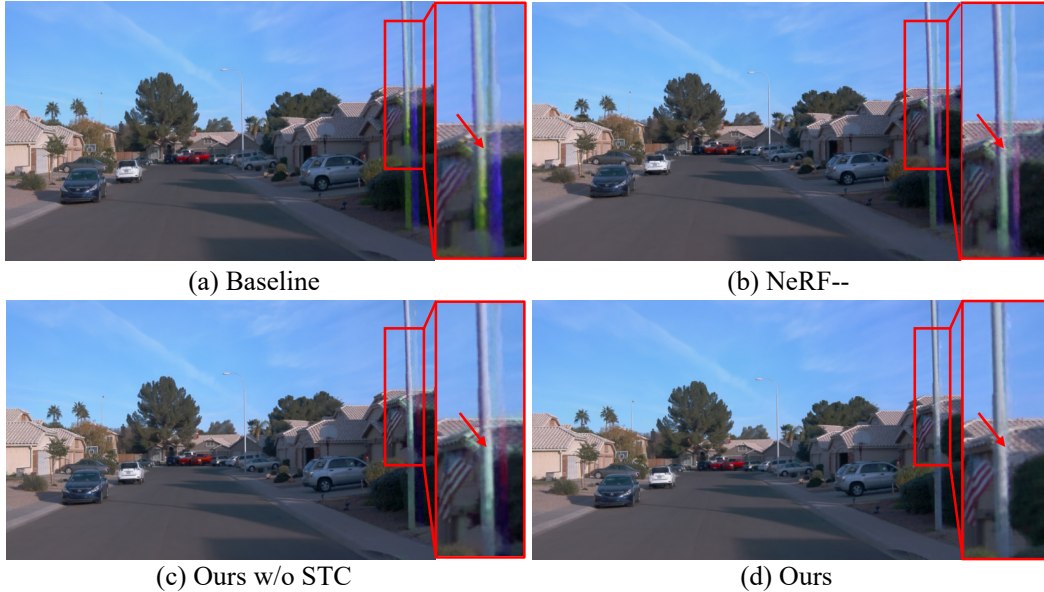


Figure 12: Quantitative comparison of different pose optimization strategies. We effectively eliminate the ghosting of the pole. STC refers to the proposed spatiotemporal constraint.

Pose Refinement Strategies S-NeRF (Xie et al. (2023)) explores the performance of various NeRF algorithms that jointly optimize poses in urban scenes and found that NeRF-- (Wang et al. (2021)) yields the best results. Thus, we compare our method with NeRF-- and validate the significance of the spatiotemporal constraint proposed in our paper. As demonstrated in Tab. 6, NeRF-- indeed enhances rendering results compared to the baseline which does not refine poses, and performance does not exhibit a significant change with the inclusion of the spatiotemporal constraint. In contrast, our spatiotemporally constrained pose refinement achieves a remarkable 238% improvement compared to NeRF--. Fig. 12 clearly demonstrates how our method effectively resolves rendering artifacts. Due to color variation among different cameras, NeRF-- struggles to achieve precise pose optimization based on the photometric error. The ghosting of the pole (b) does not change significantly compared to the baseline (a). However, when poses are optimized by explicit pixel correspondences, the ghosting is noticeably reduced (c). Furthermore, with the addition of our spatiotemporal constraint, the artifact completely disappears (d).

Table 6: Ablation study on different strategies for pose refinement. NeRF-- refine poses within the NeRF framework by photometric loss while we refine poses based on explicit pixel correspondences among images. STC refers to the proposed spatiotemporal constraint.

Method	PSNR \uparrow	SSIM \uparrow	LPIPS \downarrow
Baseline	28.09	0.851	0.374
NeRF--	28.48	0.851	0.383
NeRF-- w/ STC	28.51	0.852	0.383
Ours w/o STC	29.01	0.866	0.376
Ours	29.14	0.867	0.355

Table 7: Comparison of diverse weather conditions. (Waymo Segment-100170, Waymo Segment-150908)

Method	Rainy			Night		
	PSNR \uparrow	SSIM \uparrow	LPIPS \downarrow	PSNR \uparrow	SSIM \uparrow	LPIPS \downarrow
Zip-NeRF[3]	27.65	0.831	0.434	30.69	0.864	0.512
UC-NeRF (Ours)	30.03	0.866	0.387	31.32	0.869	0.491

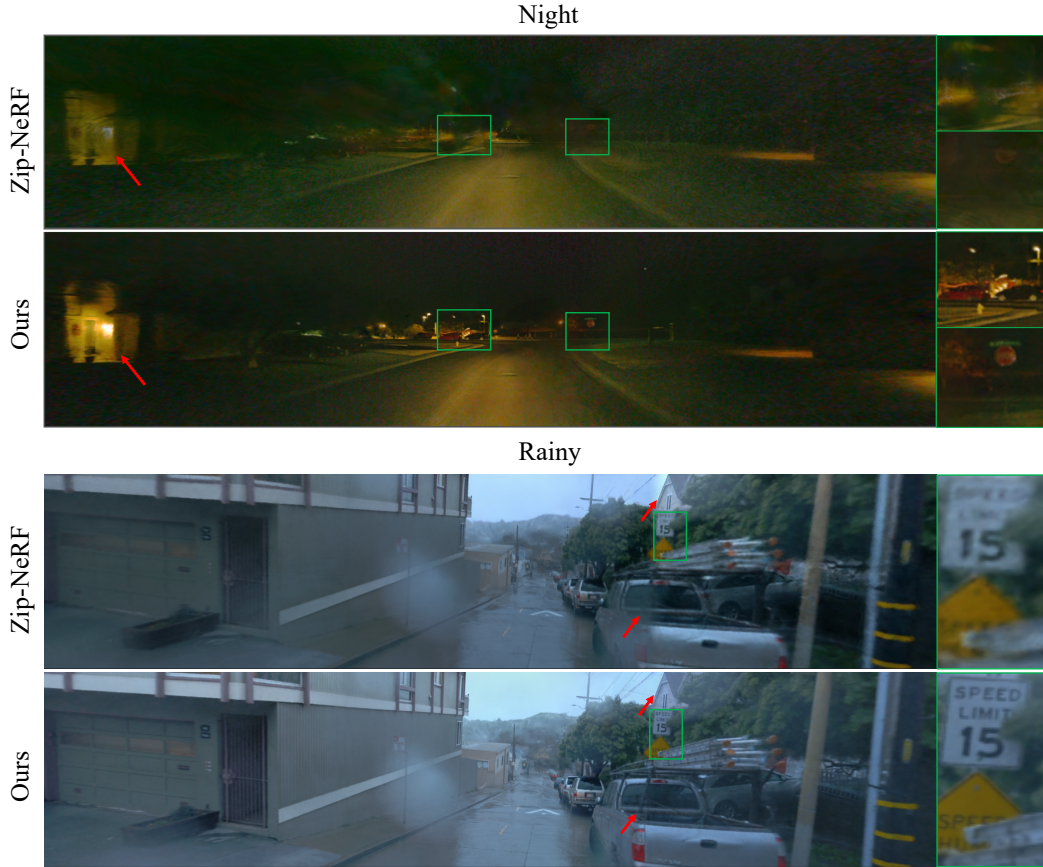


Figure 13: 180° panorama rendering results in night and rainy conditions.

Results on diverse weather conditions We further validate the robustness of our method under nighttime and rainy conditions. As shown in Tab. 7, our approach still significantly outperforms ZipNeRF in these scenarios. As illustrated in Fig. 13, we manage to eliminate the rendering artifacts caused by color inconsistency (indicated by red arrows) and achieve better rendering of details (highlighted by the green boxes).

Weight for Sky Loss As shown in Tab. 8, we compare the performance of our UC-NeRF using different weights for sky loss. Our UC-NeRF is not very sensitive to the changes in the loss weights.

Table 8: Ablation study on the weight of sky loss.

w_{sky}	PSNR \uparrow	SSIM \uparrow	LPIPS \downarrow
0	27.89	0.849	0.378
0.001	28.05	0.851	0.379
0.002	28.15	0.851	0.374
0.004	27.98	0.850	0.378

Using a large weight of sky loss might diminish the weight of the photometric loss, leading to a slight performance decline. $[0.001, 0.002]$ is the reasonable range for our loss weight.

More Results on Layer-based Color Correction As shown in Fig 14, we present additional rendering results in overlap regions of different cameras. The original NeRF exhibits significant color inconsistencies in overlapping areas. Through color correction, we are able to render images that maintain global color consistency.

More Results on Spatiotemporally Constrained Pose Refinement As shown in Fig 15, the issue of rendering artifacts and blurriness caused by pose errors is quite common in the multi-camera setup. Based on our observations, they typically occur in the overlapping regions captured by different cameras. This implies that these rendering artifacts result from errors in the relative transformations between the cameras. By explicitly modeling the relative transformations between cameras and ensuring spatiotemporal constraints during optimization, it is evident that these problems have been significantly addressed (shown in red boxes).



Figure 14: More results on color correction.



Figure 15: More results on pose refinement.

A.3.3 MORE RESULTS ON WAYMO AND NUSCENES

We further present rendering results on the Waymo and NuScenes datasets, which are compared with state-of-the-art methods S-NeRF (Xie et al. (2023)) and Zip-NeRF (Barron et al. (2023)). As shown in Fig. 16- 18, it is evident that both S-NeRF and Zip-NeRF exhibit color inconsistencies on the sides of the images, where they overlap with other cameras. In contrast, we have addressed this issue through layer-based color correction. Furthermore, we achieve improved rendering quality, such as clear contours, patterns, and text, and more accurate geometry by incorporating virtual warping and spatiotemporally constrained pose refinement.

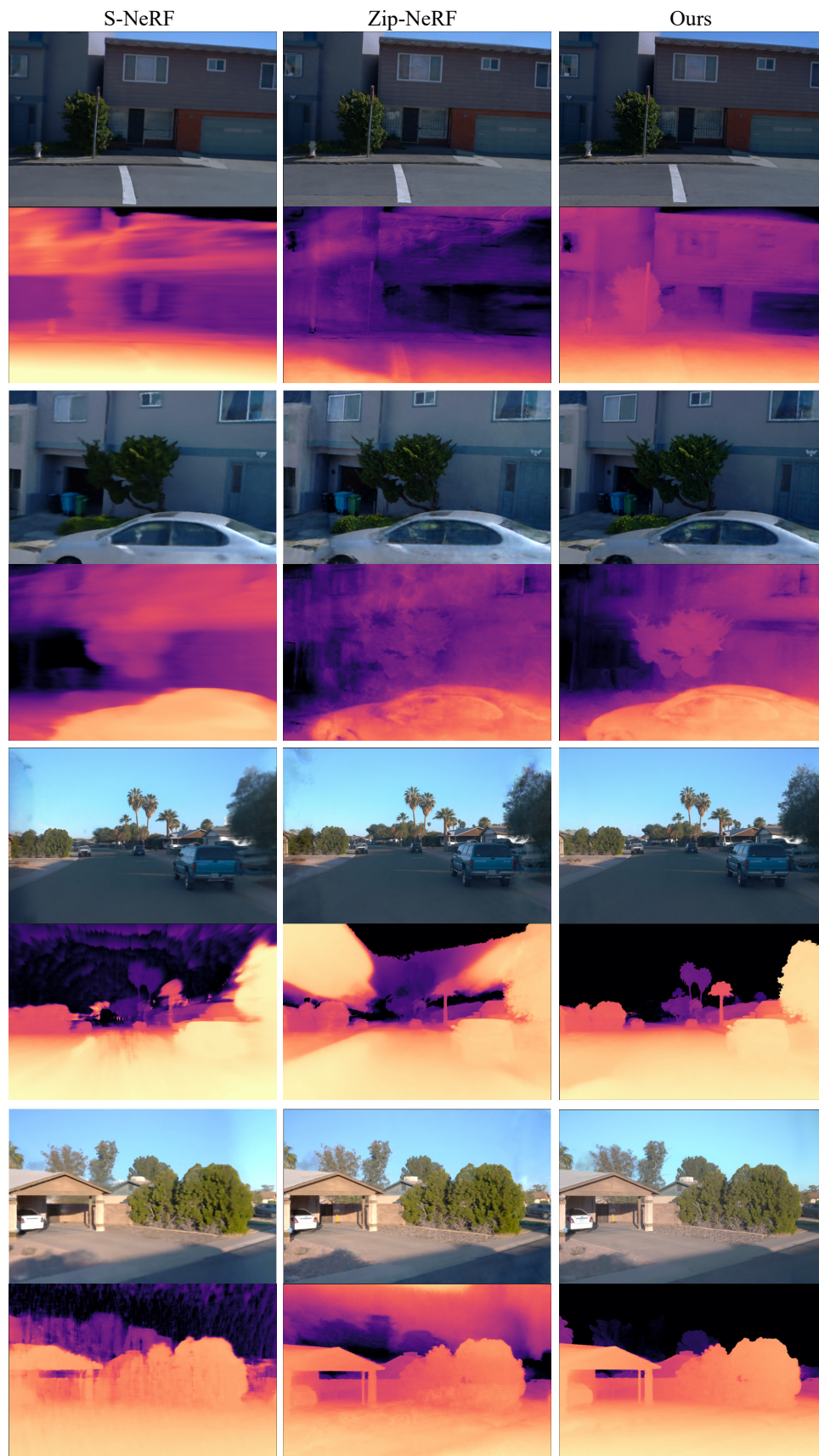


Figure 16: Comparison of the rendering results with the state-of-the-art S-NeRF and Zip-NeRF in Waymo.

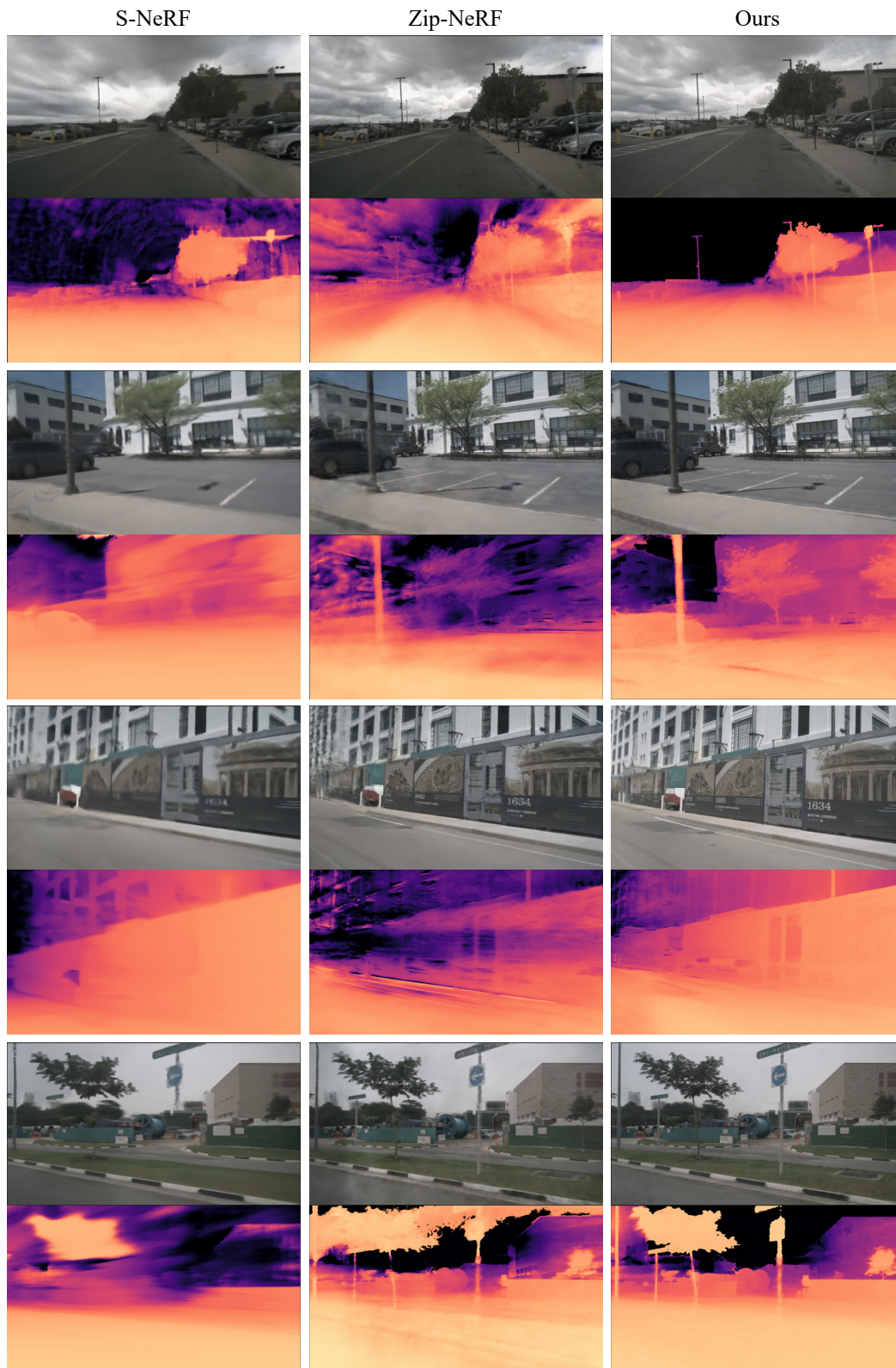


Figure 17: Comparison of the rendering results and dept maps with S-NeRF Tosi et al. (2023) (left) and Zip-NeRF Barron et al. (2023) (middle) in NuScenes.

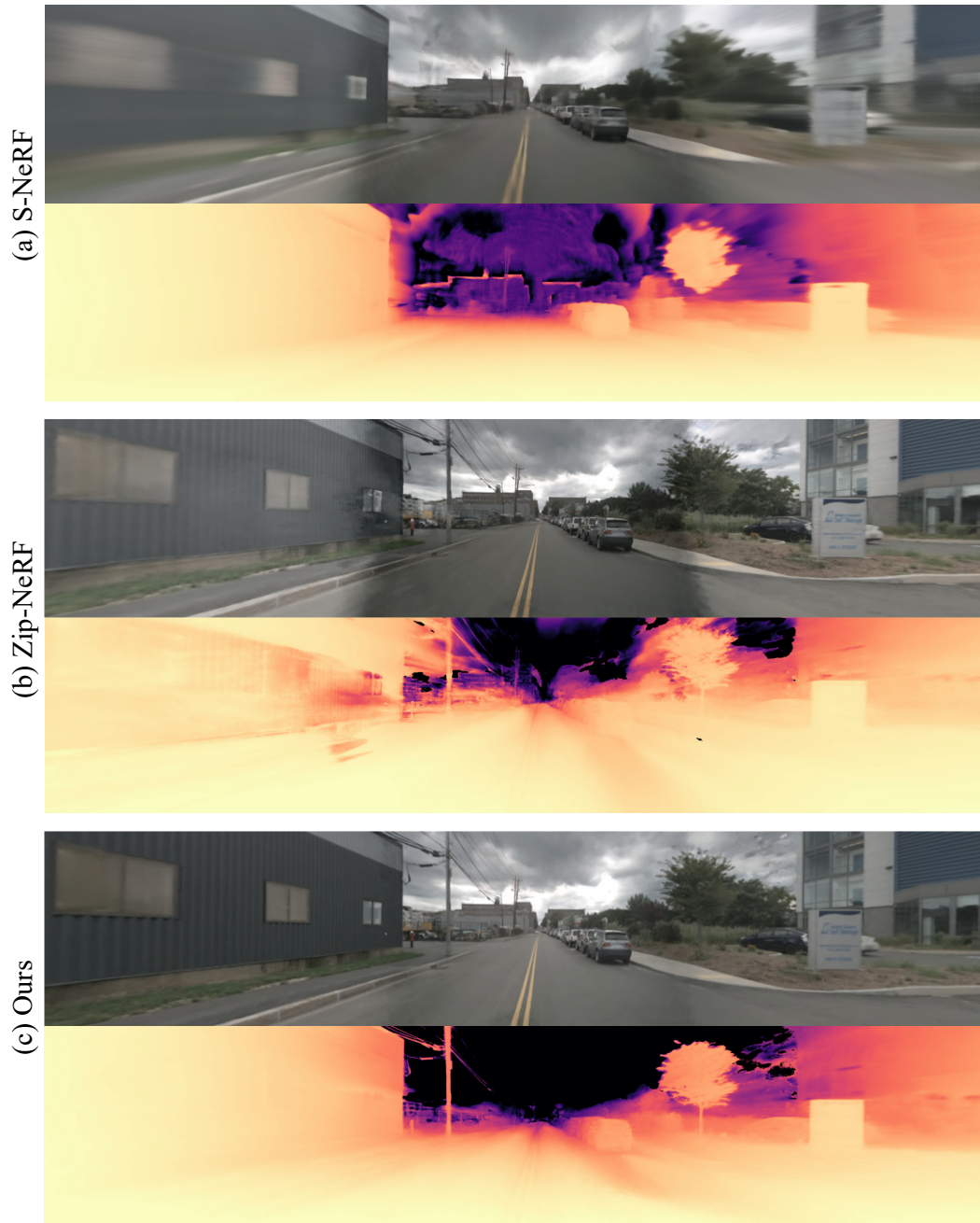


Figure 18: 180° panorama rendering results in NuScenes.